ACADEMIC PRESS

Available online at www.sciencedirect.com

SCIENCE DIRECT®

Journal of Magnetic Resonance 162 (2003) 356–363

JMR Journal of Magnetic Resonance

www.elsevier.com/locate/jmr

Flow effects in long-range dipolar field MRI

Paulo Loureiro de Sousa,* Daniel Gounot, and Daniel Grucker

Institut de Physique Biologique, Université Louis Pasteur, UMR 7004-CNRS, 4, rue Kirschléger, Strasbourg Cedex 67085, France

Received 16 October 2002; revised 23 January 2003

Abstract

Incoherent spin motion, such as diffusion, can lead to significant signal loss in multiple spin echoes (MSE) experiments, sometimes to its complete extinction. Coherent spin motion, such as laminar flow, can also modify the magnetization in MSE imaging and yield additional contrast. Our experimental results indicate that MSE is flow-sensitive. Our theoretical analysis and experimental results show how the effect of the distant dipolar field can be annihilated by flow. This effect can be quantified by directly solving the nonlinear Bloch equation, taking into account the deformation of the dipolar field by motion. Unexpected results have been observed, such as a recovery of the dipolar interaction due to flow in the ''magic angle'' condition.

Keywords: MSE; Distant dipolar field; CRAZED; Flow

1. Introduction

In highly polarized nuclear spin systems a single sequence of two r.f. pulses spaced by a delay time τ is capable of producing a train of echoes (multiple spin echoes—MSE) occurring at multiples of τ (Fig. 1a). This effect, originally observed in solid and liquid ^{3}He [1,2], has also been observed in ordinary samples such as water, at room temperature [3,4]. It has been interpreted as a consequence of the ''dipolar field'' generated by the bulk nuclear magnetization acting on the spins as an additional component of the magnetic field. This additional field makes the Bloch equation nonlinear. The solution to this modified Bloch equation can be expressed as a series of harmonics, which correspond to the multiple echoes observed.

Although the ''classical'' approach provides a correct explanation of the dipolar field effects, an alternative quantum-mechanical interpretation has been proposed [5–9]. In the ''quantum'' framework the signal arises from intermolecular multiple quantum coherences (iMQC) involving the (usually neglected) long-range dipolar spin interactions. Typically, the dipolar interaction distance (the ''correlation distance'') ranges between 10 μm and a few millimeters and can be set by appropriate experimental parameters. It has been found that signal arising from the long-range dipolar field effect depends on magnetic susceptibility variations over the correlation distance [10]. Therefore, the structure of a sample can be probed by tunning the correlation distance.

This distance-selected sensitivity mechanism presents great potentials in medical magnetic resonance imaging (MRI) [11–21]. In the past years, human brain images using iMQC [12–15] were obtained, confirming that this effect could yeld a new contrast in vivo. More recently, functional iMQC-MRI [19–21] demonstrated a different sensitivity to the BOLD (blood oxygenation level dependent) effect than conventional single quantum coherence (SQC). Long-range dipolar field MRI has also been used to enhancing diffusion-weighted MRI [22], to mapping the absolute value of the equilibrium nuclear magnetization [18] and for the characterization of trabecular bone quality [16,17].

Despite its potential utility in medical imaging, MRI using the distant dipolar field (DDF) effect has a serious drawback: a very low signal-to-noise ratio (SNR) [13], so that it is crucial to characterize the factors which affect the signal intensity. Mechanisms that induce signal decrease in iMQC, such as relaxation and diffusion, have been exhaustively studied over the last years [21–29].

* Corresponding author.
E-mail address: loureiro@ipb.u-strasbg.fr (P. Loureiro de Sousa).

1090-7807/03/$ - see front matter © 2003 Elsevier Science (USA). All rights reserved.
doi:10.1016/S1090-7807(03)00044-2

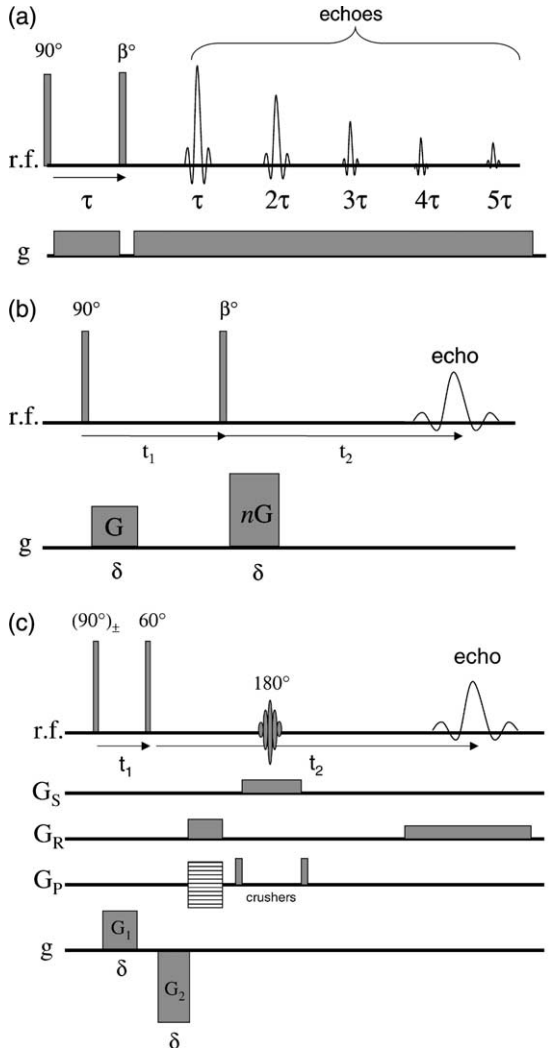

Fig. 1. Sequences used in MSE: (a) the basic MSE sequence consisting of two r.f. pulses (angle 90° and β°) and a steady gradient field; (b) the nth-order MSE sequence (or CRAZED sequence), consisting of two r.f. pulses (angle 90° and β°) and the two gradient pulses of duration δ and strength G and nG, respectively. If $t_1 = \tau$ then $t_2 = n\tau$. (c) The MSE–MRI sequence with a slice-selective refocusing (180°) pulse. Only the first pulse is phase-cycled. The gradient $\boldsymbol{g}$ can be chosen to point to any direction (cf. text for greater details).

Rizzi et al. [15] suggested that flow also might contribute to reduce the signal in iZQC (intermolecular zero quantum coherence) images of the ventricular cerebrospinal fluid (CSF). Our own preliminary anatomical iDQC (intermolecular double quantum coherence) images of rat brains at 4.7 T (unpublished) suggest a strong contrast originating from the CSF. This supposedly flow-related phenomenon prompted further investigation.

The choice between the "classical" and "quantum" treatment is usually a matter of convenience for solving a particular problem. The connection between the classical "average dipolar field" and the quantum "intermolecular dipolar spin coupling" pictures has been demonstrated by many authors [7,9,30–32]. While the "quantum" treatment is useful to optimize of pulse sequences, the "classical" treatment is more efficient to simulate real-world heterogeneous samples. Warren and co-workers have proposed a so-called "hybrid" approach to handle dipolar field effects for simulations purposes in MRI [33]. In this approach, the signal is still considered as originating from iMQC ("quantum picture") but calculations are improved by the numerical integration of the modified Bloch equation ("classical picture"). It has been suggested that flow effects in iMQC-MRI could also be dealt with through this "hybrid" approach [10]. In this paper, we present a theoretical and experimental study of flow effects in long-range dipolar field MRI. These effects can be quantified by directly solving the nonlinear Bloch equation, taking into account the deformation of the dipolar field by motion.

2. Theory

The dipolar coupling strength D_{ij} between two spins i and j scales as $D_{ij} \propto (3\cos^2\theta - 1)/2$, where θ_{ij} is the angle between the interspin vector $\boldsymbol{r}_{ij}$ and the main magnetic field $\boldsymbol{B}_0$. In an isotropic fluid an interspin vector samples all directions during an NMR time-scale experiment (typically from milliseconds to seconds), through molecular diffusion and therefore the dipolar coupling averages to zero. When the distance between the interacting spins increases, dipolar averaging through diffusion becomes less effective. In this case, the sum of interactions is averaged to zero over the sample by symmetry. It has been demonstrated that the long-range intermolecular interactions could be reintroduced by applying an external field gradient, which breaks the spherical symmetry [1,6,7]. This interaction between spins can be described by the resulting "distant dipolar field (DDF)"

$$\boldsymbol{B}_d(\boldsymbol{r}) = \frac{\mu_0}{4\pi}\int \mathrm{d}^3\boldsymbol{r}'\,\frac{1-3\cos^2\theta_{\boldsymbol{r}\boldsymbol{r}'}}{2|\boldsymbol{r}-\boldsymbol{r}'|^3}\,[3M_Z(\boldsymbol{r}')\hat{\boldsymbol{z}} - \boldsymbol{M}(\boldsymbol{r}')], \quad (1)$$

where μ_0 is the magnetic permeability constant and $\boldsymbol{M}$ the magnetization vector. In the case where a field gradient modulates the magnetization along a direction given by the unit vector $\hat{\boldsymbol{k}}$, $\boldsymbol{B}_d$ can be reduced to the much simpler form [1]

$$\boldsymbol{B}_d(\boldsymbol{r}) = \mu_0 \Lambda(\hat{\boldsymbol{k}})[M_Z(\boldsymbol{r})\hat{\boldsymbol{z}} - \boldsymbol{M}(\boldsymbol{r})/3], \quad (2)$$

where $\Lambda(\hat{\boldsymbol{k}}) = P_2(\hat{\boldsymbol{k}}\cdot\hat{\boldsymbol{z}}) = (3\cos^2\theta - 1)/2$ is the second-order Legendre polynomial of the cosine of the angle θ between the vector $\boldsymbol{k}$ and the main magnetic field. $\Lambda(\hat{\boldsymbol{k}})$ is a scale factor of DDF, which is maximal for spatial modulation along the main magnetic field direction ($\theta = 0°$) and vanishes if modulation is imposed at the "magic angle" ($\theta = 54.7°$).

The condition necessary to reduce the non-local distant dipolar field into a form that depends on the local magnetization value is the existence of a strong linear field gradient applied in a single direction [1] so that the modulation wave length is much shorter than the size of the sample. Moreover, by means of field gradients the direction of the interspin vector and the distance of spin coupling $|\boldsymbol{r}_{ij}|$ can be set as an experimental parameter. The effect of flow in MSE can be evaluated using the nonlinear Bloch equation that include the distant dipolar field (DDF)

$$\frac{\mathrm{d}\boldsymbol{M}(\boldsymbol{r})}{\mathrm{d}t} = \gamma[\boldsymbol{M}(\boldsymbol{r}) \times (\boldsymbol{B}_0 + \boldsymbol{B}_d)] = \gamma[\boldsymbol{M}(\boldsymbol{r}) \times (B_0 + \mu_0 \Lambda(\hat{\boldsymbol{k}}) M_Z(\boldsymbol{r}))\hat{\boldsymbol{z}}], \tag{3}$$

where γ is the gyromagnetic ratio. For the sake of simplifying, relaxation and diffusion are neglected in this deduction.

To perform MSE imaging, pulsed gradients have been preferred against steady-gradients. In this case only the nth-order echo is acquired. Let us consider the nth-order MSE sequence of Fig. 1b (usually known as CRAZED (COSY revamped with asymmetric z-gradient echo detection) sequence [6]). How M_z is modulated only after the second pulse, the effect of DDF during the period between the two r.f. pulses can be ignored. During the gradient time (δ), the transverse magnetization ($M_+ = M_x + \mathrm{i}M_y$) evolves as

$$M_+(\boldsymbol{r}) = M_0 \exp(\mathrm{i}\phi), \tag{4}$$

where M_0 is the equilibrium magnetization per unit volume and the phase ϕ is given by

$$\phi = \gamma \int_0^{\delta} \boldsymbol{g} \cdot \boldsymbol{r}(t')\, \mathrm{d}t'. \tag{5}$$

Dephasing by spin motion can be taken into account expanding ϕ in a Taylor series

$$\phi = \gamma \boldsymbol{r}_0 \cdot \int_0^{\delta} \boldsymbol{g}(t')\, \mathrm{d}t' + \gamma \boldsymbol{v} \cdot \int_0^{\delta} \boldsymbol{g}(t') t'\, \mathrm{d}t' + \cdots = \gamma \boldsymbol{m}_0 \cdot \boldsymbol{r}_0 + \gamma \boldsymbol{m}_1 \cdot \boldsymbol{v} + \cdots, \tag{6}$$

where $\boldsymbol{m}_0$ and $\boldsymbol{m}_1$ are the zeroth and the first gradient moment, respectively, and $\boldsymbol{r}_0$ and $\boldsymbol{v}$ are the position and velocity of each spin. For a gradient pulse applied during the time interval from t_i to t_f, the gradient moment is defined by

$$\boldsymbol{m}_k = \int_{t_i}^{t_f} \boldsymbol{g}(t) t^k\, \mathrm{d}t. \tag{7}$$

During the time delay $t_1 - \delta$ the spins move over the distance $\Delta\boldsymbol{r} = \boldsymbol{v}(t_1 - \delta)$ and the magnetization changes into $M(\boldsymbol{r}) \to M(\boldsymbol{r} + \Delta\boldsymbol{r})$. We can still use Eq. (4) to describe the transverse magnetization, with ϕ given by

$$\phi = \gamma \boldsymbol{m}_0 \cdot \{\boldsymbol{r}_0 - \Delta\boldsymbol{r}\} + \gamma \boldsymbol{m}_1 \cdot \boldsymbol{v}, \tag{8}$$

$$= \gamma \boldsymbol{m}_0 \cdot \{\boldsymbol{r}_0 - \boldsymbol{v}(t_1 - \delta)\} + \gamma \boldsymbol{m}_1 \cdot \boldsymbol{v}. \tag{9}$$

Immediately after the second r.f. pulse of angle β, magnetization is given by

$$M_z(t_1^+) = -M_0 \cos\phi \sin\beta, \tag{10}$$

$$M_+(t_1^+) = M_0 \cos\phi \cos\beta + \mathrm{i}M_0 \sin\phi. \tag{11}$$

In a CRAZED sequence a refocusing gradient is applied after the second r.f. pulse (Fig. 1b). The second gradient has an area n times that of the first gradient before the r.f. pulse, to excite MSE of order n. Further to the second r.f. pulse, the spin system evolves over the distant dipolar field (DDF). In the absence of flow, DDF changes slowly under the combined influence of nuclear spin lattice relaxation and diffusion. In the presence of flow, $\boldsymbol{M}_z$ is also modified by spin translation and $\boldsymbol{M}_+$ will precess in a time-dependent DDF over the t_2 period.

Considering that the second gradient has no effect over the longitudinal magnetization, and since there are no more r.f. pulses, M_z can still be described using Eq. (10) at the time $t \geqslant t_1$

$$M_z(\boldsymbol{r}, t) = -M_0 \cos\phi \sin\beta, \tag{12}$$

where

$$\phi(\boldsymbol{r}, t) = \gamma \boldsymbol{m}_0 \cdot \{\boldsymbol{r}_0 - \boldsymbol{v}(t - \delta)\} + \gamma \boldsymbol{m}_1 \cdot \boldsymbol{v}. \tag{13}$$

During the second gradient time δ the transverse magnetization evolves according to

$$M_+(\boldsymbol{r}, t_1 + \delta) = M_+(\boldsymbol{r}, t_1^+) \exp\{\mathrm{i}\phi'(\boldsymbol{r})\}, \tag{14}$$

where $\phi'(\boldsymbol{r}, t_1 + \delta) = \gamma \boldsymbol{m}_0' \cdot \boldsymbol{r}_0 + \gamma \boldsymbol{m}_1' \cdot \boldsymbol{v}$. The zeroth and the first moment of the second gradient ($\boldsymbol{m}_0'$ and $\boldsymbol{m}_1'$, respectively) are calculated between t_1 and $t_1 + \delta$. Flow will increase the spatial dephasing ϕ' during t_2 as: $\phi'(\boldsymbol{r}) \to \phi'(\boldsymbol{r} + \boldsymbol{v}(t_2 - \delta))$. Then, at the detection time $t = t_1 + t_2$ the magnetization is given by

$$M_z(\boldsymbol{r}, t) = -M_0 \cos\phi \sin\beta, \tag{15}$$

$$M_+(\boldsymbol{r}, t) = (M_0 \cos\phi \cos\beta + \mathrm{i}M_0 \sin\phi) \exp(\mathrm{i}\phi'), \tag{16}$$

where

$$\phi(\boldsymbol{r}, t) = \gamma \boldsymbol{m}_0 \cdot \{\boldsymbol{r}_0 - \boldsymbol{v}(t - \delta)\} + \gamma \boldsymbol{m}_1 \cdot \boldsymbol{v}, \tag{17}$$

$$\phi'(\boldsymbol{r}, t) = \gamma \boldsymbol{m}_0' \cdot \{\boldsymbol{r}_0 - \boldsymbol{v}(t_2 - \delta)\} + \gamma \boldsymbol{m}_1' \cdot \boldsymbol{v}. \tag{18}$$

Using M yielded by Eqs. (15) and (16), the Bloch equation (Eq. (3)) can now be solved taking into account the DDF modification throughout the evolution time ($t > t_1$). At the detection time $t = t_1 + t_2$, we find

$$M_+(\boldsymbol{r}, t) = (M_0 \cos\phi \cos\beta + \mathrm{i}M_0 \sin\phi) \exp(\mathrm{i}\phi') \times \exp\{\mathrm{i}\gamma\mu_0 \bar{\Lambda}(\hat{\boldsymbol{k}}) M_z(t) t\}, \tag{19}$$

where $\bar{\Lambda}(\hat{\boldsymbol{k}}) = \int_{t_1}^{t_2} \Lambda(\hat{\boldsymbol{k}}(t))\, \mathrm{d}t$. The unit vector $\hat{\boldsymbol{k}}$ in $\Lambda(\hat{\boldsymbol{k}})$ points in the direction of the $\boldsymbol{M}_z$ modulation. $\boldsymbol{k}$ and ϕ are related by $\boldsymbol{k} = \nabla\phi$.

A close look at Eq. (17) indicates that in the simple case where there is no bulk flow ($\boldsymbol{v} = 0$) and G is the strength of the linear field gradient $\boldsymbol{g}$ applied for a time δ

along the direction of unit vector $\hat{\boldsymbol{s}}$, $\boldsymbol{k}$ is related to the zeroth moment $\boldsymbol{m}_0 = G\delta\hat{\boldsymbol{s}}$ as $\boldsymbol{k} = \boldsymbol{k}_0 = \gamma\boldsymbol{m}_0$. In this case, $\Lambda(\hat{\boldsymbol{k}}) = \Lambda(\hat{\boldsymbol{s}})$ and it depends only on the direction of $\boldsymbol{g}$. But, if $\boldsymbol{v} \neq 0$, we can write $\boldsymbol{k} = \boldsymbol{k}_0 + \boldsymbol{k}_1$ where $\boldsymbol{k}_1 = G\delta t\nabla(\hat{\boldsymbol{s}} \cdot \boldsymbol{v})$ and $t = (3/2)\delta - t_1 - t_2$. For a system where the local velocity gradient is significant compared to the reciprocal of t, then $\boldsymbol{k}_1$ is not negligible compared to $\boldsymbol{k}_0$. In this system, $\Lambda(\hat{\boldsymbol{k}})$ is no longer controlled by the direction of $\boldsymbol{g}$ alone, but depends also on $\nabla\boldsymbol{v}$, the spatial velocity variation.

In order to quantify MSE in the presence of flow, let us substitute for $\boldsymbol{M}_z$ from Eq. (15) into Eq. (19)

$$M_+(\boldsymbol{r},t) = (M_0\cos\phi\cos\beta + \mathrm{i}M_0\sin\phi)\exp(\mathrm{i}\phi') \times \exp\{-\mathrm{i}\gamma\mu_0\bar{\Lambda}(\hat{\boldsymbol{k}})M_0 t\cos\phi\sin\beta\}. \quad (20)$$

By applying the Bessel function identity to Eq. (20)

$$\mathrm{e}^{\mathrm{i}\xi\cos\phi} = \sum_{m=-\infty}^{m=+\infty} \mathrm{i}^m J_m(\xi)\mathrm{e}^{\mathrm{i}m\phi}, \quad (21)$$

we find

$$M_+(\boldsymbol{r},t) = (M_0\cos\phi\cos\beta + \mathrm{i}M_0\sin\phi)\exp(\mathrm{i}\phi') \times \sum_{m=-\infty}^{m=+\infty} \mathrm{i}^m J_m(-\xi)\mathrm{e}^{\mathrm{i}m\phi}, \quad (22)$$

where $\xi = (\bar{\Lambda}(\hat{\boldsymbol{k}})t/\tau_{\mathrm{D}})\sin\beta$, and $\tau_{\mathrm{D}} = (\gamma\mu_0 M_0)^{-1}$ is the dipolar demagnetizing time [8]. We can replace $\cos\phi$ and $\sin\phi$ by the trigonometric identities $\cos\phi = (\mathrm{e}^{\mathrm{i}\phi} + \mathrm{e}^{-\mathrm{i}\phi})/2$ and $\sin\phi = (\mathrm{e}^{\mathrm{i}\phi} - \mathrm{e}^{-\mathrm{i}\phi})/2\mathrm{i}$:

$$M_+(\boldsymbol{r},t) = \frac{M_0}{2}\left(\mathrm{e}^{\mathrm{i}\phi}(\cos\beta+1) + \mathrm{e}^{-\mathrm{i}\phi}(\cos\beta-1)\right)\mathrm{e}^{\mathrm{i}\phi'} \times \sum_{m=-\infty}^{m=+\infty} \mathrm{i}^m J_m(-\xi). \quad (23)$$

Defining $\phi^* \equiv \phi'/n - \phi = 2\gamma G\delta t_1(\hat{\boldsymbol{s}} \cdot \boldsymbol{v})$, then ϕ^* can be withdrawn from the summation

$$M_+(\boldsymbol{r},t) = \frac{M_0}{2}\mathrm{e}^{\mathrm{i}n\phi^*} \times \sum_{m=-\infty}^{m=+\infty} [\mathrm{e}^{\mathrm{i}(m+n+1)\phi}(\cos\beta+1) + \mathrm{e}^{\mathrm{i}(m+n-1)\phi}(\cos\beta-1)]\mathrm{i}^m J_m(-\xi)\mathrm{e}^{\mathrm{i}m\phi}. \quad (24)$$

Since ϕ depends on the absolute position $\boldsymbol{r}$, averaging over the sample causes the signal to vanish unless $m = -n \pm 1$. The resulting signal can then be written as

$$M_+(\boldsymbol{r},t) = \frac{M_0}{2}\mathrm{e}^{\mathrm{i}m\phi^*} \times [\mathrm{i}^{-(n+1)}(\cos\beta+1)J_{-(n+1)}(-\xi) + \mathrm{i}^{-(n-1)}(\cos\beta-1)J_{-(n-1)}(-\xi)]. \quad (25)$$

Using the properties of the Bessel function [8], after some mathematical manipulations, we finally obtain

$$M_+(\boldsymbol{r},t) = M_0\mathrm{i}^{-(n+1)} \{nJ_n(\xi)/\xi + 0.5[J_{n-1}(\xi) - J_{n+1}(\xi)]\cos\beta\}\mathrm{e}^{\mathrm{i}n\phi^*}. \quad (26)$$

This is the same result as in [29], multiplied by a phase shift $\mathrm{e}^{\mathrm{i}n\phi^*}$. This phase shift can introduce imaging artifacts in MSE–MRI as in usual non-flow-compensated SE–MRI. By using first-order flow-compensated sequences it is possible to eliminate these artifacts in SE and MSE [35]. However, the deformation of the distant dipolar field by flow cannot be avoided. Hence, the loss of signal in MSE–MRI due to flow is a direct consequence of the modification of $\Lambda(\hat{\boldsymbol{k}})$.

In order to describe more precisely the effect of flowing spins on MSE imaging, let us examine the simple case of laminar flow. In our experiments, flow is expected to obey Poiseuille's law and to have a parabolic velocity profile (in cylindrical coordinates): $\boldsymbol{v}(\rho) = v_{\max}(1 - \rho^2/\rho_0^2)\hat{\boldsymbol{z}}$, where ρ_0 is the cylinder radius and $v_{\max}$ is the maximal velocity at the center of the parabolic radial profile. In MSE–MRI, it is usual to set the encode gradient $\boldsymbol{g}$ to the z-direction, that corresponds to the maximal value of Λ in the absence of flow. Using the results obtained for ϕ in Eq. (17), yielding $\boldsymbol{k} = \boldsymbol{k}_0 + \boldsymbol{k}_1 = \nabla\phi$ and imposing $\boldsymbol{g} = G\hat{\boldsymbol{z}}$, we have:

$$\boldsymbol{k}_0 = \gamma G\delta\hat{\boldsymbol{z}}, \quad (27)$$

$$\boldsymbol{k}_1 = \gamma G\delta(2t_1 + 2t_2 - 3\delta)v_{\max}(\rho/\rho_0^2)\hat{\boldsymbol{\rho}}. \quad (28)$$

The angle θ between vector $\boldsymbol{k}$ and the main magnetic field is then given by

$$\theta = \tan^{-1}\left(\frac{(2t_1 + 2t_2 - 3\delta)v_{\max}}{\rho_0}\frac{\rho}{\rho_0}\right). \quad (29)$$

Fig. 2 illustrates the dependence of θ and $\Lambda(\hat{\boldsymbol{k}})$ with an adimensional parameter $v_{\max}t/\rho_0$ along of the normalized radius ρ/ρ_0, calculated from Eq. (29). At $\rho = \rho_0$ the angle θ between vector $\boldsymbol{k}$ and $\boldsymbol{B}_0$ may grow as a function of $v_{\max}t/\rho_0$. When $v_{\max}t = \rho_0$, θ varies gradually up to 45° as function of its radial position. Then, the decrease in MSE signal due the modified θ and Λ may be important in laminar flow when $v_{\max}$ is of the same order of magnitude as ρ_0/t where $t = 2t_1 + 2t_2 - 3\delta$.

3. Methods

3.1. Experimental set-up

Experiments were carried-out in a 4.7 T SMIS small animal imager, with a 200 mm in diameter horizontal-bore magnet (MR Research Systems, UK), using a 10-cm long, 40-mm-diameter bird-cage r.f. coil. The phantom used in these experiments consisted of a 6-m long flexible tube of circular cross-section (outer diameter 12 mm and inner diameter 8 mm) in which gadolinium-doped distilled water ($T_2 \sim T_1 \simeq 100$ ms) was circulated. The steady flow mode in the tube was obtained by keeping constant the difference in height

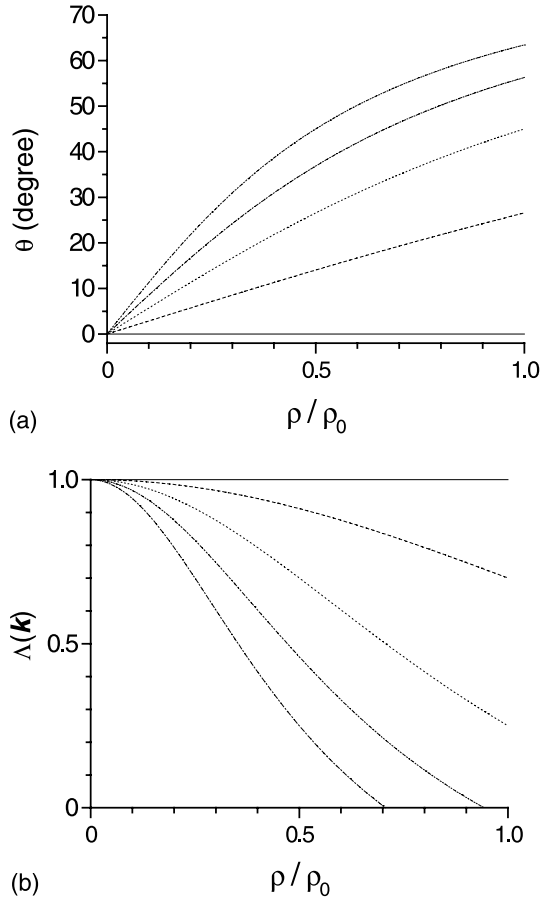

Fig. 2. Simulation of the main parameters of the distant dipolar field in a laminar flow. (a) Calculated variation of θ, the angle between the vector $\boldsymbol{k}$ and $\hat{\boldsymbol{z}}$, as a function of the normalized radial position ρ/ρ_0 to a Poiseuille flow where ρ_0 is the center of the tube. Each line corresponds to distinct values of the adimensional parameter $v_{\max}t/\rho_0$ from Eq. (29): (–) 0, (––) 0.5, (···) 1, (–·–) 1.5, (–··–) 2. (b) Calculated variation of $\Lambda = (3\cos^2\theta - 1)/2$, using θ values obtained in (a).

between two reservoirs, in permanent overflow [34]. Flow rates were calibrated from 1.3 to 13.4 ml/s, which corresponds to mean velocities of 2.5–27.4 cm/s.

The second-order MSE–MRI sequence was performed by adding a slice-selective 180° refocusing pulse and standard spin-warp imaging gradients to the basic CRAZED sequence (Fig. 1c). Imaging was carried-out by selecting a plane normal to the flow direction. The relevant pulse sequence parameters for MSE–MRI were the following: matrix size = 64 × 128, TR = 2 s, NEX = 4 (with phase cycling of the first r.f. pulse), field of view (FOV) of 14 × 14 mm, slice thickness of 20 mm, $t_1 = 2.0$ ms, $t_2 = 34$ ms, $\delta = 1.4$ ms, β r.f. pulse = 60°, $G_2 = -2 \times G_1 = 145$ mT/m. SE images were taken as control, by setting $G_1 = -G_2 = 145$ mT/m. Signal attenuation through diffusion is negligible (<1%) for the combined experimental parameters (t_1, δ, G_1, and G_2). Data were analyzed with MATLAB (MathWorks, MA).

3.2. Simulations

In order to understand our results, we simulated second-order MSE imaging in the presence of a laminar flow. The distant dipolar magnetic field was calculated for an (infinite) cylindrical sample of radius ρ_0 and a spatially modulated magnetization $\boldsymbol{M}$ moving in a direction parallel to $\boldsymbol{B}_0$, with a parabolic distribution of velocities. The MSE signal intensity (Eq. (26)) depends on the scale factor Λ, which is yielded by $\Lambda(\hat{\boldsymbol{k}}) = (3\cos^2\theta - 1)/2$. θ was calculated at each radial position using Eq. (29). The experimental values used in our simulations were $\rho_0 = 4$ mm, $\delta = 1.4$ ms, $t_1 = 2$ ms, $t_2 = 34$ ms, $G_2 = -2 \times G_1 = 145$ mT/m, $\tau_D = 200$ ms ($B_0 = 4.7$ T), and $\beta = 60°$.

4. Results and discussion

A selection of MSE and SE images is shown in Figs. 3a–d. Figs. 3a and b show images of stationary water for SE and MSE, respectively, while Figs. 3c and d show images with flow. No apparent change is noticeable in SE images whether with or without flow, while in the MSE images there is a clear contrast induced by motion

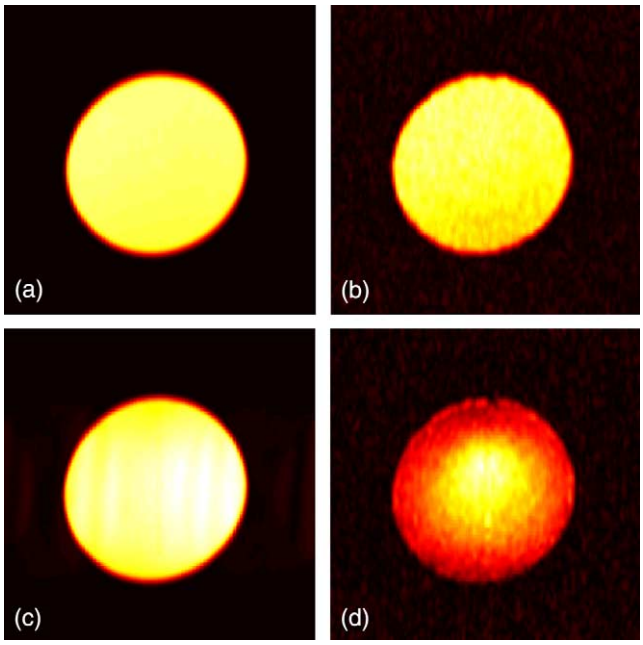

Fig. 3. Comparison of conventional (SE) images and multiple spin echoes (MSE) images. (a) SE and (b) MSE images of stationary fluid using the sequence shown in Fig. 1c. Signal-to-noise ratios were 158 and 64, respectively. (c) SE and (d) MSE images of laminar fluid flow ($v_{\max} = 5$ cm/s), using the same sequence as (a) and (b). MSE images were obtained by setting $G_2 = -2 \times G_1 = 145$ mT/m, while in SE images $G_2 = -G_1 = 145$ mT/m, keeping the other parameters constant (t_1, t_2, δ, TR, FOV, and matrix size). Relevant pulse sequence parameters for MSE–MRI are described in Section 3. Images have been normalized to their maximum intensity.

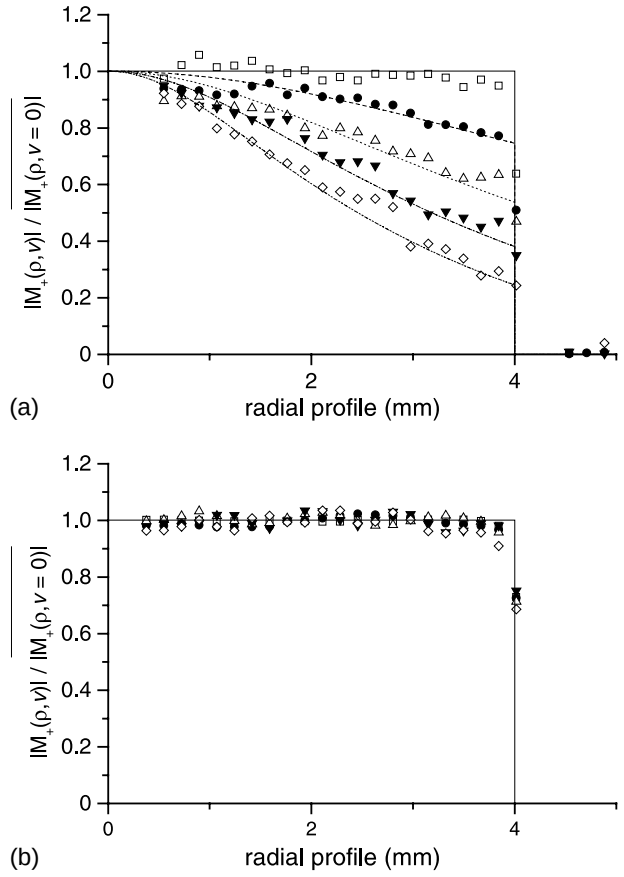

Fig. 4. Comparison of experimental (symbols) and simulated data (lines) from radial profiles obtained to (a) MSE and (b) SE images of laminar fluid flow, to five distinct v_{max} values (in cm/s). simulation data: (–) 0, (––) 5, (· · ·) 8, (– · –) 10.8, and (– · · –) 14; experimental data: (□) 0, (●) 5, (△) 8, (▼) 10.8, and (◇) 14. Simulation data were obtained from Eqs. (26) and (29). Absolute signal intensities $|M_+(\rho, v)|$ were normalized by the mean intensity of the respective images without flow $\overline{|M_+(\rho, v = 0)|}$.

(d). This contrast can be quantified using our previous theoretical approach.

Figs. 4a and b show experimental and simulated radial profiles from MSE and SE images, respectively, for five distinct velocities. Data were normalized by the mean intensity of the respective images without flow. The effects of relaxation and diffusion are cancelled by this normalization since the experimental parameters (t_1, t_2, G, δ, TR, FOV, and matrix size) were kept constant. Simulated curves were calculated as described in Section 3. The difference between experimental and simulated results is less than ~5%. This error originates in great part from flow instability during acquisition and from artifacts due to the non-flow-compensated MRI sequences used.

Unexpected results have been observed when the angle Θ between the encode gradient $\boldsymbol{g}$ and the main field $\boldsymbol{B}_0$ is set to 54.7°, the "magic angle." In the 'magic angle' condition, the scale factor Λ is expected to be equal to zero throughout the sample and the image must vanish. Fig. 5 shows MSE images obtained by setting $\Theta = 54.7°$. In the case where $\boldsymbol{v} = 0$ the signal vanishes throughout the image except for the border region, where susceptibility artifacts can hinder complete signal annihilation. In the case where $\boldsymbol{v} \neq 0$, we observed an asymmetric signal recovery in the image. This recovery grows more important as velocity increases.

In order to explain this strange behavior let us write down the Cartesian components of $\boldsymbol{k} = \nabla\phi$ taking into account an arbitrary direction to $\boldsymbol{g}$ given by $\boldsymbol{g} = G(\sin\Theta\hat{\boldsymbol{x}} + \cos\Theta\hat{\boldsymbol{z}})$ with $\boldsymbol{v} = v_{max}(1 - (x^2 + y^2)/\rho_0^2)\hat{\boldsymbol{z}}$

$$\boldsymbol{k}_x = k_0[\sin\Theta + \cos\Theta(2t_1 + 2t_2 - 3\delta)v_{max}x]\hat{\boldsymbol{x}}, \tag{30}$$

$$\boldsymbol{k}_y = k_0[\cos\Theta(2t_1 + 2t_2 - 3\delta)v_{max}y]\hat{\boldsymbol{y}}, \tag{31}$$

$$\boldsymbol{k}_z = k_0\cos\Theta\hat{\boldsymbol{z}}, \tag{32}$$

where $k_0 = \gamma G\delta$. The angle θ between vector $\boldsymbol{k}$ and the main magnetic field is then yielded by

$$\theta = \tan^{-1}\left(\frac{\sqrt{k_x^2 + k_y^2}}{k_z}\right). \tag{33}$$

In experiments where $\Theta = 0°$, MSE flow images display a cylindrical symmetry because $\boldsymbol{k}_\rho$, the spatial phase

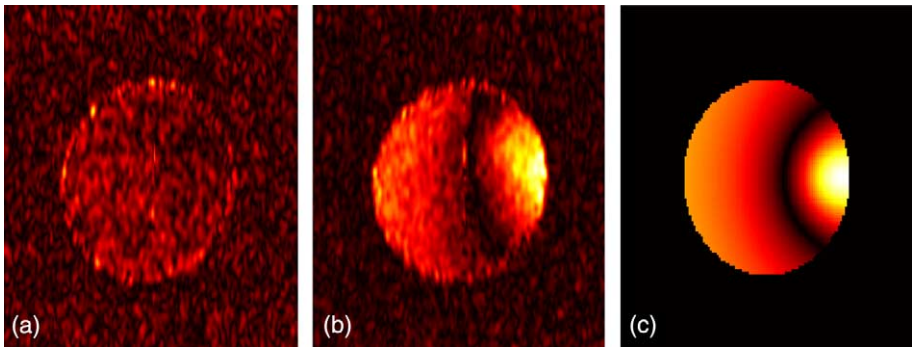

Fig. 5. MSE image in the "magic angle" condition ($\Theta = 54.7°$) of a stationary fluid (a) and a Poiseuille fluid flow (b). Simulation of MSE image of the flow in the "magic angle" condition is displayed on (c). In both (experimental and simulated) images v_{max} was set to 15 cm/s. Images have been normalized to their maximum intensity.

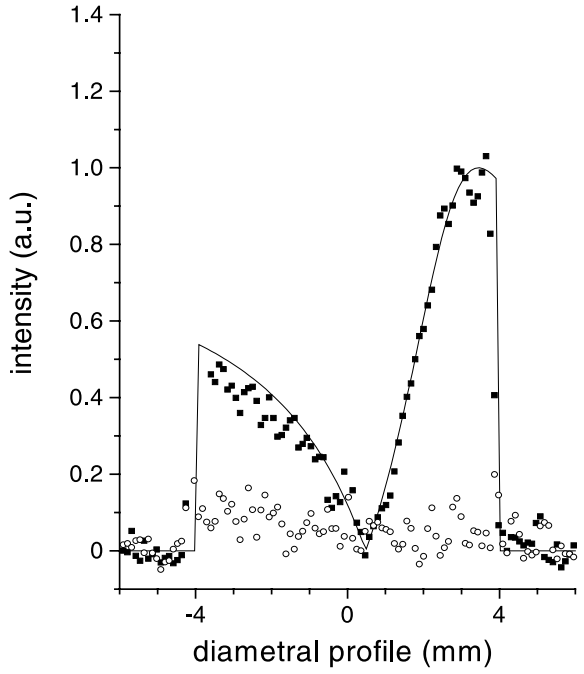

Fig. 6. Experimental (symbols) data from diametrical profiles obtained from the images displayed in Fig. 5: (◯) stationary fluid and (■) laminar flow. The line is a profile taken from the simulated image in Fig. 5.

variation, is symmetrical around z. In the 'magic angle' experiments, introducing an additional modulation k_x (since $g = G(\sin\Theta\hat{x} + \cos\Theta\hat{z})$) breaks this cylindrical symmetry.

Fig. 5c shows a simulation of a MSE image of laminar flow under the 'magic angle' condition. The MSE signal was calculated using Eq. (26), with θ and Λ calculated from Eqs. (30)–(33), setting $\Theta = 54.7°$. Fig. 6 shows the profiles of simulated (Fig. 5c) and experimental images (Figs. 5a and b). An excellent agreement was obtained between experimental and simulated data.

5. Conclusion

Our theoretical analysis and experimental results have shown how the signal in MSE–MRI can be annihilated or created (in magic angle conditions) by flow. This new effect has been interpreted as a modification of the DDF orientation by velocity gradients of flowing spins. First- or higher-order flow-compensated sequences are unable to avoid loss of signal in MSE. We believe that the results and conclusions could be useful to help interpreting in vivo images, where loss of signal due to flow could be mistaken for contrast due to other causes (e.g., relaxation).

However, the contrast in MSE–MRI arising from the velocity gradients could be used to obtain information about blood perfusion at an intravoxel scale, providing an indirect access to the capillary perfusion which is a major indicator of local brain activation. Therefore, this effect should be complementary to the susceptibility effect in functional MSE imaging. Further work should tell us whether as many developments are likely to 'spin off' from this contrast as those used in magnetic resonance angiography.

Apart from medical applications, material systems, such as porous media [36–39], in which important variations in spin velocity are encountered, should also benefit from this new contrast in MSE–MRI.

Acknowledgments

The authors thank Dr. J. Baruthio for excellent assistance with the experimental set-up, Dr. M. Engelsberg, Dr. R. Bowtell, and Dr. B. Foester for helpful discussions. This work was supported by the *Contrat de Plan Etat – Région Alsace 2000–2006* and the *Hôpitaux Universitaires de Strasbourg*.

References

[1] G. Deville, M. Bernier, J.M. Delrieux, NMR multiple echoes observed in solid ^{3}He, Physical Review B 19 (1979) 5666–5688.
[2] D. Einzel, G. Eska, Y. Hirayoshi, T. Kopp, P. Wölfle, Multiple spin echoes in a normal Fermi liquid, Physical Review Letters 53 (1984) 2312–2315.
[3] R. Bowtell, R.M. Bowley, P. Glover, Multiple spin echoes in liquids in a high magnetic field, Journal of Magnetic Resonance 88 (1990) 643–651.
[4] R. Bowtell, S. Gutteridge, C. Ramanathan, Imaging the long-range dipolar field in structured liquid state samples, Journal of Magnetic Resonance 150 (2001) 147–155.
[5] Q. He, W. Richter, S. Vathyam, W.S. Warren, Intermolecular multiple-quantum coherences and cross correlations in solution nuclear magnetic resonance, The Journal of Chemical Physics 98 (1993) 6779–6800.
[6] W.S. Warren, W. Richter, A.H. Andreotti, B.T. Farmer II, Generation of impossible cross-peaks between bulk water and biomolecules in solution NMR, Science 262 (1993) 2005–2009.
[7] S. Lee, W. Richter, S. Vathyam, W.S. Warren, Quantum treatment of the effects of dipole–dipole interactions in liquid nuclear magnetic resonance, The Journal of Chemical Physics 105 (1996) 874–900.
[8] W. Richter, W.S. Warren, Intermolecular multiple quantum coherences in liquids, Concepts in Magnetic Resonance 12 (2000) 396–409.
[9] E.D. Minot, P.T. Callaghan, N. Kaplan, Multiple echoes, multiple quantum coherence, and the dipolar field: demonstrating the significance of higher order terms in the equilibrium density matrix, Journal of Magnetic Resonance 140 (1999) 200–205.
[10] L.-S. Bouchard, R.R. Rizzi, W.S. Warren, Magnetization structure contrast based on intermolecular multiple-quantum coherences, Magnetic Resonance in Medicine 48 (2002) 973–979.
[11] A. Bifone, G.S. Payne, M.O. Leach, In vivo multiple spin echoes, Journal of Magnetic Resonance 135 (1998) 30–36.
[12] W.S. Warren, S. Ahn, M. Mescher, M. Garwood, K. Ugurbil, W. Richter, R.R. Rizi, J. Hopkins, J.S. Leigh, MR imaging contrast enhancement based on intermolecular zero quantum coherences, Science 281 (1998) 247–251.

[13] J. Zhong, Z. Chen, E. Kwok, In vivo intermolecular double-quantum imaging on a clinical 1.5 T MR scanner, Magnetic Resonance in Medicine 43 (2000) 335–341.
[14] J. Zhong, Z. Chen, E. Kwok, New image contrast mechanisms in intermolecular double-quantum coherence in human MR imaging, Journal of Magnetic Resonance Imaging 12 (2000) 311–320.
[15] R.R. Rizi, S. Ahn, D.C. Alsop, S. Garrett-Roe, M. Mescher, W. Richter, M.D. Schnall, J.S. Leigh, W.S. Warren, Intermolecular zero-quantum coherence imaging of the human brain, Magnetic Resonance in Medicine 43 (2000) 627–632.
[16] S. Capuani, F. Curzi, F.M. Alessandri, B. Maraviglia, A. Bifone, Characterization of trabecular bone by dipolar demagnetizing field MRI, Magnetic Resonance in Medicine 46 (2001) 683–689.
[17] S. Capuani, F.M. Alessandri, A. Bifone, B. Maraviglia, Multiple spin echoes for the evaluation of trabecular bone quality, Magnetic Resonance Materials in Biology, Physics, and Medicine 14 (2002) 3–9.
[18] S. Gutteridge, C. Ramanathan, R. Bowtell, Mapping the absolute value of M_0 using dipolar field effects, Magnetic Resonance in Medicine 47 (2002) 871–879.
[19] J. Zhong, Z. Chn, W.E. Kwok, S. Kennedy, Z. You, Optimization of blood oxygenation level-dependent sensitivity in magnetic resonance imaging using intermolecular double-quantum coherence, Journal of Magnetic Resonance Imaging 16 (2002) 733–740.
[20] W. Richter, M. Richter, W.S. Warren, H. Merkle, P. Andersen, G. Adriany, K. Ugurbil, Functional magnetic resonance imaging with intermolecular multiple-quantum coherences, Magnetic Resonance Imaging 18 (2000) 489–494.
[21] J. Zhong, E. Kwok, Z. Chen, fMRI of auditory stimulation with intermolecular double-quantum coherences (iDQCs) at 1.5 T, Magnetic Resonance in Medicine 43 (2001) 356–364.
[22] J. Zhong, Z. Chen, E. Kwok, S. Kennedy, Enhanced sensitivity to molecular diffusion with intermolecular double-quantum coherences: implications and potential applications, Magnetic Resonance Imaging 19 (2001) 33–39.
[23] Z. Chen, Z. Chen, J. Zhong, Quantitative study of longitudinal relaxation related to intermolecular dipolar interactions in solution NMR, Chemical Physics Letters 333 (2001) 126–132.
[24] H. Zhang, N. Lizitsa, R.G. Bryant, W.S. Warren, Experimental characterization of intermolecular multiple-quantum coherence pumping efficiency in solution NMR, Journal of Magnetic Resonance 148 (2001) 200–208.
[25] J. Zhong, Z. Chen, S. Zheng, S.D. Kennedy, Theoretical and experimental characterization of NMR transverse relaxation process related to intermolecular dipolar interactions, Chemical Physics Letters 350 (2001) 260–268.
[26] I. Ardelean, E. Kossel, R. Kimmich, Attenuation of homo- and heteronuclear multiple spin echoes by diffusion, The Journal of Chemical Physics 114 (2001) 8520–8529.
[27] Z. Chen, J. Zhong, Unconventional diffusion behaviors of intermolecular multiple-quantum coherences in nuclear magnetic resonance, The Journal of Chemical Physics 114 (2001) 5642–5653.
[28] S. Garrett-Roe, W.S. Warren, Numerical studies of intermolecular multiple quantum coherences: High-resolution NMR in inhomogeneous fields and contrast enhancement in MRI, Journal of Magnetic Resonance 146 (2000) 1–13.
[29] Z. Chen, S.D. Kennedy, J. Zhong, Quantitation of intermolecular dipolar effects in NMR spectroscopy and high order MSE MR imaging, Magma 11 (2000) 122–128.
[30] J. Jeener, Equivalence between the classical and the "Warren" approaches for the effects of long range dipolar couplings in liquid nuclear magnetic resonance, The Journal of Chemical Physics 112 (2000) 5091–5094.
[31] J. Jeener, Collective effects in liquid NMR: dipolar field and radiation damping, in: D.M. Grant, R.K. Harris (Eds.), Supplement of the Encyclopedia of Nuclear Magnetic Resonance, Wiley, New York, 2002, pp. 642–679.
[32] M.H. Levitt, Demagnetization field effects in two-dimensional solution NMR, Concepts in Magnetic Resonance 8 (1996) 77–103.
[33] T. Enss, S. Ahn, W.S. Warren, Visualizing the dipolar field in solution NMR and MR imaging: three-dimensional structure simulation, Chemical Physics Letters 305 (1999) 101–108.
[34] M. Stevanov, J. Baruthio, D. Gounot, Arterial compliance and pulse pressure MR measurements: an optimized procedure combining a phase contrast multi movie and a 1D technique, Computers in Cardiology 26 (1999) 363–366.
[35] A. Jerschow, N. Müller, Convection compensation in gradient enhanced nuclear magnetic resonance spectroscopy, Journal of Magnetic Resonance 132 (1998) 13–18.
[36] S. Capuani, M. Alesiani, F.M. Alessandri, B. Maraviglia, Characterization of porous media structure by non linear NMR methods, Magnetic Resonance Imaging 19 (2001) 319–323.
[37] R. Bowtell, P. Robyr, Structural investigations with the dipolar demagnetizing field in solution NMR, Physical Review Letters 76 (1996) 4971–4974.
[38] P. Robyr, R. Bowtell, Nuclear magnetic resonance microscopy in liquids using the dipolar field, The Journal of Chemical Physics 106 (1997) 467–476.
[39] F.M. Alessandri, S. Capuani, B. Maraviglia, Multiple spin echoes in heterogeneous system: physical origins of the observed dips, Journal of Magnetic Resonance 156 (2002) 72–78.

Further reading

[1] I. Ardelean, R. Kimmich, Diffusion measurements using the nonlinear stimulated echo, Journal of Magnetic Resonance 143 (2000) 101–105.
[2] I. Ardelean, R. Kimmich, Diffusion measurements with the pulsed gradient nonlinear spin echo method, The Journal of Chemical Physics 112 (2000) 5275–5280.